Journal of Materials Chemistry A

ROYAL SOCIETY OF CHEMISTRY

PAPER

View Article Online
View Journal

Cite this: DOI: 10.1039/d5ta08003g

A bromine-rich artificial interphase to regulate interfacial kinetics in boron-centered electrolytes for magnesium metal batteries

Deviprasath Chinnadurai, †*[a] Gaoliang Yang,†*[a] Sonal Kumar,[a] Shengnan Sun,[a] Jianbiao Wang,[a] Zhenxiang Xing,[a] Debbie Hwee Leng Seng,[a] Zdenek Sofer[b] and Zhi Wei Seh*[a]

Rechargeable magnesium batteries (RMBs) have emerged as promising next-generation energy storage systems owing to their high volumetric energy density and inherent safety. However, the passivation of magnesium (Mg) anodes and irregular Mg deposition in conventional electrolytes severely limit their reversibility and long-term cycling stability. Although advanced boron-centered electrolytes enable reversible Mg plating/stripping without anode passivation, interfacial challenges and irregular Mg deposition still persist, compromising cycling stability and coulombic efficiency (CE). Here, we design a bromine-rich artificial interphase on a Mg anode (Br-Mg) that effectively mitigates interfacial challenges and regulates deposition homogeneity. The Br-Mg anode demonstrated an extended cycling life of 1610 hours in a symmetric cell, while maintaining a low voltage hysteresis of only ±68 mV, a substantial improvement from 796 hours and ±145 mV for bare Mg. Furthermore, the CE of the Mg plating/stripping process measured in an asymmetric cell increased from 96.47% with bare Mg to 99.50% with the Br-Mg anode, with extended cycling life from 380 cycles to 1630 cycles. The superior electrochemical performance is attributed to favorable interfacial kinetics imparted by the Br-rich interphase, which ensures high ionic mobility and suppresses electrolyte-induced degradation. In a full-cell configuration with a Mo_6S_8 cathode, the Br-Mg anode delivered stable cycling and high capacity. This study provides a strategic design concept for creating efficient artificial interphases on Mg anodes to improve reversibility and CE in boron-centered Mg electrolytes.

Received 30th September 2025
Accepted 13th January 2026

DOI: 10.1039/d5ta08003g

rsc.li/materials-a

[a]Institute of Materials Research and Engineering (IMRE), Agency for Science, Technology and Research (A*STAR), 2 Fusionopolis Way, Innovis #08-03, Singapore 138634, Republic of Singapore. E-mail: deviprasath_chinnadurai@a-star.edu.sg; yang_gaoliang@a-star.edu.sg; sehzw@a-star.edu.sg

[b]Department of Inorganic Chemistry, University of Chemistry and Technology, Prague, Technická 5, Prague 616628, Czech Republic

† These authors contributed equally to this work.

Deviprasath Chinnadurai

*Dr Deviprasath Chinnadurai is a Scientist at the Institute of Materials Research and Engineering (IMRE), Agency for Science, Technology and Research (A*STAR), Singapore. He received his PhD in Electrical Engineering from Pusan National University, South Korea, in 2020. Following his PhD, he continued as a postdoctoral fellow at Pusan National University before moving to Gyeongsang National University, South Korea, where he held a postdoctoral position until 2021. In 2022, he joined A*STAR, Singapore, as a Scientist. His current research is dedicated to the design of advanced electrolytes and interfacial engineering strategies for post-lithium-ion batteries, with particular emphasis on rechargeable magnesium and aluminium-ion batteries.*

Introduction

Rechargeable magnesium batteries (RMBs) have emerged as a promising alternative to lithium-ion batteries owing to the intrinsic advantages of magnesium (Mg) metal anodes, including high volumetric capacity, low reduction potential, and natural abundance.[1,2] Despite these merits, the practical deployment of RMBs remains severely hindered by the passivation of Mg anodes in conventional electrolytes.[3,4] Such passivation layers obstruct ionic transport, leading to higher overpotentials, poor reversibility, and unstable cycling performance. Consequently, significant research efforts have been devoted to the design of advanced electrolyte systems capable of enabling efficient and reversible Mg plating/stripping.

Early electrolyte systems for RMBs were predominantly based on nucleophilic complex chemistries,[5–7] whereas, in recent years, non-nucleophilic systems[8–10] have emerged as far more promising candidates. Nevertheless, these systems still rely heavily on electrolyte engineering strategies such as additive modification[11–20] and solvent optimization,[21–26] to enable passivation-free Mg plating/stripping. Among these, the most effective formulations to date have predominantly incorporated chloride-containing additives.[11,16–18,27–32] While such electrolytes facilitate ionic transport and improve interfacial charge transfer, their reliance on Cl^- coordination intrinsically narrows the electrochemical stability windows and promotes corrosive side reactions at current collectors and other cell components. These limitations pose a fundamental barrier to the realization of high-voltage RMBs and significantly restrict the broader applicability. To overcome these challenges, strategies that decouple Mg reversibility from chloride-dependent chemistry are urgently required. In this context, the deliberate construction of artificial interphases has emerged as a powerful and versatile approach to enable reversible Mg cycling in non-nucleophilic electrolytes.[33–44] By engineering tailored interfacial layers, it becomes possible to suppress Mg anode passivation while simultaneously enhancing interfacial charge-transfer kinetics and long-term stability.

Alternatively, boron-centered, chloride-free electrolytes have recently emerged as a promising class of electrolyte systems for RMBs, exhibiting non-passivating behaviour toward Mg metal anodes.[45,46] These electrolytes offer several key advantages, including wide anodic stability windows and compatibility with electrophilic organic polymers and conversion-type cathodes. Nevertheless, their practical deployment remains constrained by limited cycling stability and modest coulombic efficiencies (CEs, 95–98%).[47–49] The poor cycling life and low CE of boron-centered electrolytes predominantly arise from irregular Mg deposition, undesirable side reactions (including solvent and anion decomposition), and the formation of fragile solid-electrolyte interphases (SEIs).[46,50]

Among the emerging boron-centred electrolytes for RMBs, magnesium tetrakis(hexafluoroisopropyloxy)borate (Mg$[B(hfip)_4]_2$) in 1,2-dimethoxyethane (DME) has shown the greatest promise. However, this Mg$[B(hfip)_4]_2$/DME system continues to face critical challenges, most notably the formation of an unstable and non-uniform SEI, arising from the decomposition of the strongly chelated $[Mg(DME)_3]^{2+}$ cation.[51] Efforts to address these issues have largely focused on additive engineering[48,52–54] and solvent optimization,[51] yet such strategies frequently compromise bulk electrolyte properties, including ionic conductivity and anodic stability. In parallel, the fabrication of artificial interphases on the Mg anode has emerged as an attractive approach to stabilize the SEI in Mg$[B(hfip)_4]_2$/DME without altering the bulk electrolyte composition.[55,56] These engineered interphases suppress electrolyte decomposition at the anode–electrolyte interface and promote uniform Mg deposition, thereby enhancing cycling stability to some extent. Nevertheless, the CEs of Mg plating/stripping in these systems remain restricted (96.9–97.5%), underscoring that even advanced interphase engineering falls short of resolving interfacial instabilities and achieving near-ideal reversibility. This persistent limitation highlights the pressing need for deeper mechanistic understanding and more refined design strategies to fully unlock the potential of boron-centered electrolytes, particularly Mg$[B(hfip)_4]_2$/DME for high-performance RMBs.

In this work, for the first time we report the fabrication of a Br-rich artificial interphase on a Mg anode *via* a facile dip-coating method using 1-bromopropane to address the reversibility and CE limitations of Mg$[B(hfip)_4]_2$/DME electrolyte. To the best of our knowledge, a Br-based interphase has not been previously reported with boron-centered electrolytes for RMBs. The Br-rich interphase enhances surface electrochemical kinetics, subsequently improving Mg plating/stripping reversibility in symmetric cells from 796 to 1610 hours. In asymmetric cells, the CE of the Mg plating/stripping process is significantly improved from 96.47% to 99.50%, accompanied by an increase in cycling life from 380 to 1630 cycles. Both the cycling life and CE achieved with the Br-Mg anode represent the highest values reported to date for boron-centered electrolytes. Post-mortem analyses further reveal that the artificial interphase governs deposition morphology, yielding highly homogeneous Mg growth. Moreover, full-cell evaluations with the Mo_6S_8 cathode demonstrate superior capacity and cycling stability, underscoring the effectiveness of this strategy in advancing the practical deployment of high-performance RMBs.

Experimental

Fabrication of a Br-rich artificial interphase on a Mg anode

Commercial Mg foil (99.9% purity, 0.1 mm thickness, MTI) was mechanically polished with a clean blade inside an Ar-filled glovebox until a shiny, contaminant-free surface was obtained. The polished Mg foil was used as the control sample in all comparative studies and is hereafter referred to as bare Mg. For the fabrication of the artificial interphase, pieces of polished Mg foil were punched into Ø12.7 mm discs and immersed in a reaction solution consisting of 2 vol% 1-bromopropane (99% purity, Sigma-Aldrich) in DME (99.5% purity, Sigma-Aldrich) for 1 h. Following treatment, the electrodes were thoroughly rinsed with pure DME to remove residual species to obtain Br-rich artificial interphase enabled Mg anodes, hereafter referred to as Br-Mg.

Material characterization

Detailed information about material characterization is provided in the SI.

Electrochemical measurements

Detailed information about electrochemical measurements is provided in the SI.

Results and discussion

A schematic illustration of the Br-rich artificial interphase fabrication procedure is shown in Fig. 1a, with detailed steps provided in the Experimental section. In general, organic halides (RX, X = Br, Cl, I) undergo reaction with metallic Mg in ethereal solvents to yield the corresponding Grignard reagent (eqn (1)).[41]

$$RBr + Mg \xrightarrow{DME} RMgBr \quad (1)$$

The initially formed RMgBr species ends up in Schlenk equilibrium with the generation of diorganomagnesium (R_2Mg) and magnesium dihalide ($MgBr_2$) (eqn (2)).[57,58]

$$2RMgBr \rightleftarrows R_2Mg + MgBr_2 \quad (2)$$

The concomitant organic residues generated during this process are removed through solvent washing with DME, leaving largely $MgBr_2$ on the Mg anode surface.

The successful formation of an artificial interphase on the Mg anode surface was confirmed by both digital photographs and scanning electron microscopy (SEM) images (Fig. 1b). For comparison, corresponding images of bare Mg were also obtained, highlighting clear morphological differences and confirming the successful formation of the artificial interphase on Br-Mg. Cross-sectional SEM imaging further corroborates the formation of a Br-Mg interphase on the Mg anode surface, revealing a uniform interfacial layer with an average thickness of approximately 35 μm (Fig. S1). To further elucidate the crystal structure of the interphase, X-ray diffraction (XRD) measurements were conducted on both bare Mg and Br-Mg anodes. The diffraction pattern of bare Mg matched that of pure magnesium metal (JCPDS no. 35-0821). In contrast, the Br-Mg anode exhibited an additional diffraction peak at 20.9° (JCPDS no. 74-1040), which can be indexed to $MgBr_2$, thereby confirming the successful formation of the Br-rich artificial interphase (Fig. 1c and d)).[59]

To understand and differentiate the surface chemical composition of the artificial interphase, both bare Mg and Br-Mg anodes were investigated by X-ray photoelectron spectroscopy (XPS) and time-of-flight secondary ion mass spectrometry (TOF-SIMS) techniques. The XPS peak fitting and quantitative analyses were performed using CasaXPS software (Casa Software Ltd). The quantification was carried out based on an average matrix relative sensitivity factor, considering the peak areas and the atomic sensitivity factors of the identified components. A Shirley background was applied for all fittings, and the minimum number of components was used to achieve satisfactory fits.[60] All spectra were charge-corrected by

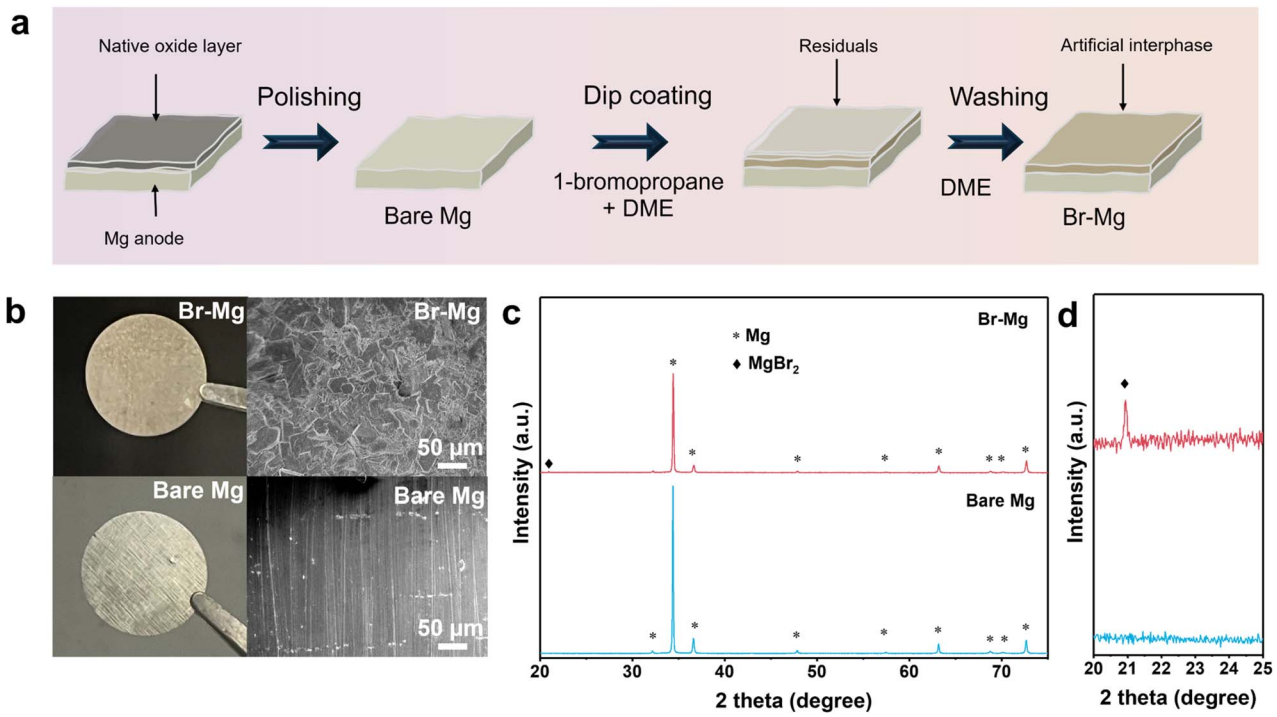

Fig. 1 (a) Schematic representing the preparation of the bare Mg and Br-Mg anodes. (b) Digital and SEM images of bare Mg and Br-Mg anodes. (c and d) XRD patterns of bare Mg and Br-Mg anodes.

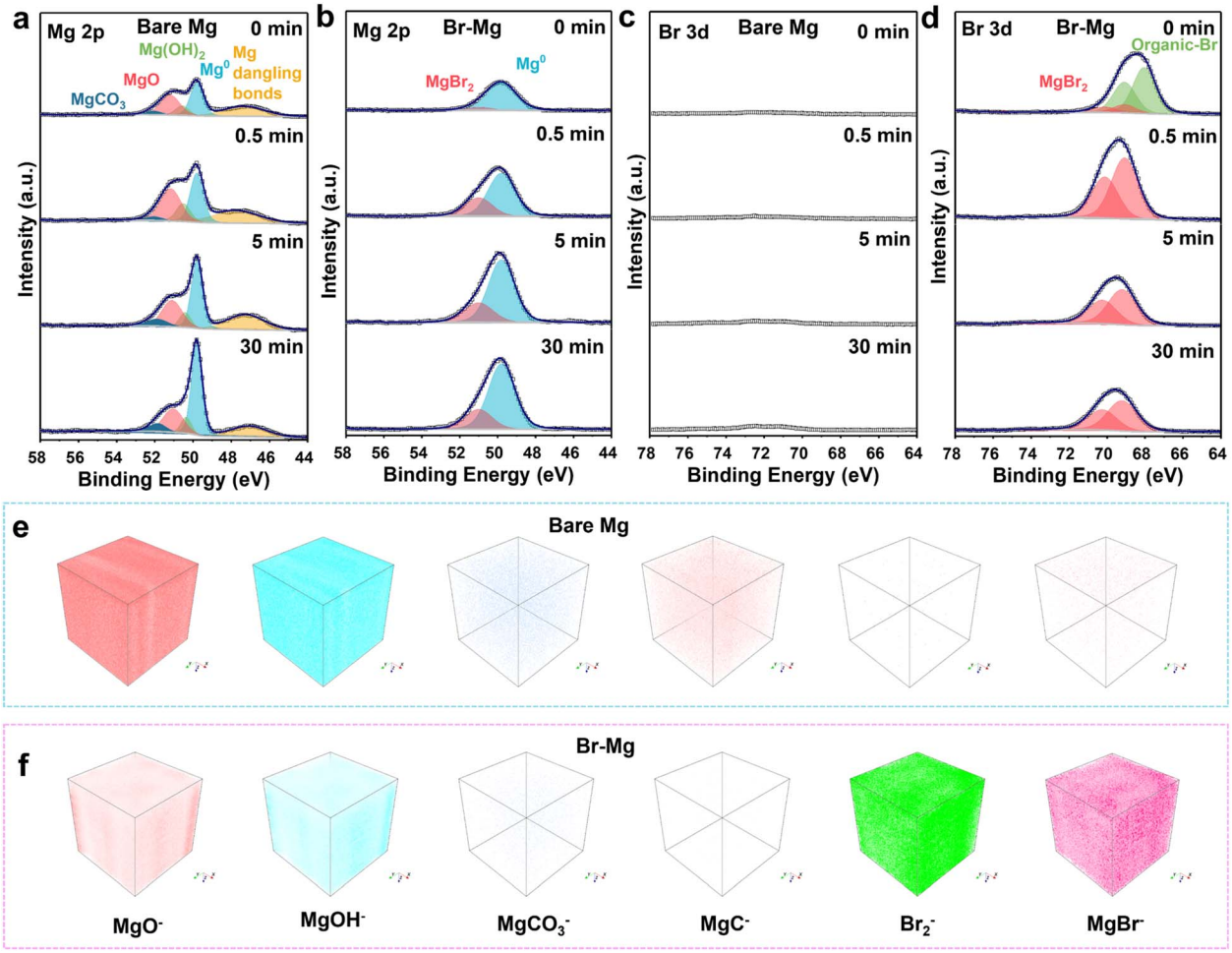

Fig. 2 Chemical and elemental composition studies of bare Mg and Br-Mg anodes. (a–d) Depth profiling XPS spectra. (e and f) 3D-rendered TOF-SIMS images.

referencing to the Mg^0 peak at 49.8 eV. The Mg 2p XPS spectra of bare Mg (Fig. 2a and Table S1) can be deconvoluted into Mg^0 (49.8 eV), $Mg(OH)_2$ (50.6 eV), MgO (51.3 eV), $MgCO_3$ (52 eV) and Mg dangling bonds (47 eV).[4,61] As $MgBr_2$ and MgO display overlapping binding energies in the Mg 2p spectra, their individual contributions cannot be clearly distinguished. Nevertheless, the featureless Br 3d spectra (Fig. 2c) of the bare Mg anode exclude the presence of $MgBr_2$ and confirm the presence of MgO on the bare Mg anode. Additionally, the high concentration of dangling bonds further confirms that the surface has higher Mg–O terminations. The Mg 2p spectra of the Br-Mg anode (Fig. 2b and Table S1) exhibit the presence of $MgBr_2$ species at all etching depths, confirming the formation of the homogeneous Br-rich artificial interphase. Also, the absence of peaks related to dangling bonds at any etching time confirms that the interphase is largely free from oxide species. The Br 3d peaks of the Br-Mg anode (Fig. 2d and Table S2) show a higher concentration of organic-Br species on the surface which diminished completely at an etching time of 0.5 min confirming that the bulk interphase does not contain any organic species. Instead, the $MgBr_2$ concentration increased drastically at an etching time of only 0.5 min confirming the presence of the inorganic $MgBr_2$-rich artificial interphase.

The 3D rendered TOF-SIMS images (Fig. 2e and f) further validated the observations from the XPS depth profiling analysis. Bare Mg shows higher concentration of MgO^- fragments; in contrast, the Br-Mg anode shows an extremely low concentration of MgO^- fragments (Fig. 2e). Instead, the Br-Mg anode exhibited high concentration of Br species (Br_2^- and $MgBr^-$), which validates the formation of a robust Br-rich artificial interphase that largely protects the anode from the formation of native oxides (Fig. 2f). Furthermore, the bare Mg anode also shows the presence of other Mg species such as $MgOH^-$, $MgCO_3^-$ and MgC^- whereas Br-Mg shows very low signals of these species. This confirms that the artificial interphase is highly homogenous in the atomic distribution of Br species, and bare Mg contains passivating Mg oxide species, specifically rich in MgO^- fragments. Generally, $MgBr_2$ has high Mg^{2+} ion mobility with a Mg migration barrier value as low as 0.14 eV in contrast to MgO which has poor ionic conductivity (Mg migration barrier value of 2.03 eV).[4]

To elucidate the beneficial role of the Br-rich artificial interphase in regulating electrochemical behaviour, interfacial

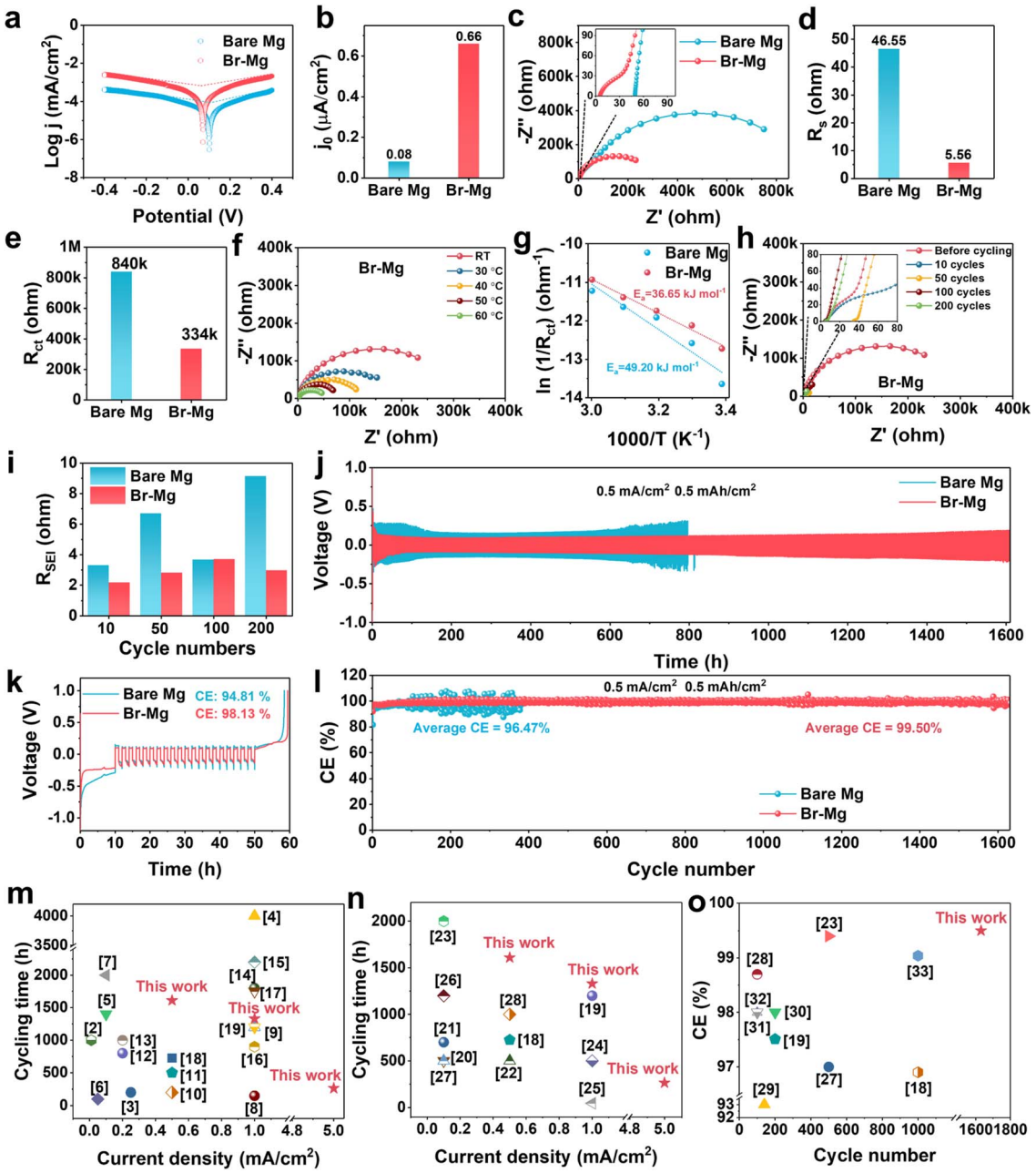

Fig. 3 Interfacial electrochemical kinetics and Mg plating/stripping reversibility of bare Mg and Br-Mg anodes. (a) Tafel curves of symmetric cells. (b) Measured exchange current density (j_0) from Tafel curves. (c) EIS Nyquist plot of symmetric cells. (d) R_s values measured from Nyquist plots. (e) R_{ct} values measured from Nyquist plots. (f) Nyquist plots of the Br-Mg symmetric cell at different temperatures. (g) Arrhenius plots with measured activation energies. (h) Nyquist plots of the Br-Mg symmetric cell at different cycling states. (i) Graphical representation of R_{SEI} measured at different cycles. (j) Galvanostatic cycling profiles of symmetric cells at 0.5 mA cm^{-2} and 0.5 mAh cm^{-2}. (k) Galvanostatic cycling profile of the asymmetric cells during the Aurbach test. (l) CE *versus* cycle number of asymmetric cells during a long term cycling test at 0.5 mA cm^{-2} and 0.5 mAh cm^{-2}. (m) Comparison of symmetric cell performances of the Br-Mg anode with previously reported artificial interphases for Mg anodes. Related data are collected from Table S6. (n) Comparison of symmetric cell performances of the Br-Mg anode with previously reported boron-centered electrolytes. Related data are collected from Table S7. (o) Comparison of asymmetric cell performance of the Br-Mg anode with previously reported boron-centered electrolytes. Related data are collected from Table S8. The reference numbers in (m–o) refer to references in the SI.

electrochemical kinetics governing Mg plating/stripping were probed through Tafel analysis and electrochemical impedance spectroscopy (EIS). The symmetric cells of bare Mg and Br-Mg were used for Tafel and EIS measurements in $Mg[B(hfip)_4]_2$/DME electrolyte. The Tafel plots (Fig. 3a) and corresponding exchange current density (j_0) (Fig. 3b) generally demonstrate the ion transport kinetics of the plating/stripping process.[62] The measured j_0 for Br-Mg (0.66 μA cm^{-2}) is much higher than that

of the bare Mg (0.08 μA cm^{-2}), indicating faster kinetics at the microelectrode surface. The low j_0 for bare Mg indicates that a larger overpotential is required to drive Mg plating/stripping, which can be correlated with the presence of passivating species at the anode–electrolyte interface. As a result, the electrolyte fails to refill the consumed Mg^{2+} near the electrode surface, leading to concentration gradient-induced Mg dendrite growth during prolonged cycling, which will ultimately cause cell short-circuiting. The EIS Nyquist plots of bare Mg and Br-Mg (Fig. 3c) are fitted using the equivalent circuits presented in Fig. S2a and S2b, respectively. The equivalent circuit employed to fit bare Mg included a series/electrolyte resistance (R_s), a charge transfer resistance (R_{ct}), and a constant phase element (CPE1). Meanwhile, the equivalent circuit employed to fit Br-Mg was composed of an additional resistance component (R_{SEI}) and constant phase element (CPE2), attributed to the presence of an artificial interphase that function as a SEI. The bare Mg exhibited a high R_s of 46.55 Ω, which drastically reduced to 5.56 Ω for Br-Mg (Fig. 3d and Table S3). Similarly, the R_{ct} of bare Mg is 8.40×10^5 Ω which reduced to 3.34×10^5 Ω for Br-Mg (Fig. 3e). The significantly lower R_s and R_{ct} values for the Br-Mg anode indicate enhanced charge-transfer kinetics at the electrode–electrolyte interface, provided by the artificial interphase. Furthermore, the Mg ion transport properties at the interface were investigated by temperature dependent EIS study.[44] The Nyquist plots measured at different temperatures (Fig. 3f and S3a) reveal that increasing the EIS measurement temperature leads to a decrease in R_{ct}, demonstrating that Mg^{2+} desolvation is a thermally activated process (Table S4).[63,64] The activation energy (E_a) of the interfacial reaction was calculated by using the Arrhenius eqn (3).

$$1/R_{ct} = A \exp(-E_a/RT) \quad (3)$$

where R_{ct} is the charge transfer resistance, A is the pre-exponential factor, R is the universal gas constant, and T is the absolute temperature.[55,65] The E_a values were determined by the slope of the linear fit of $\ln(R_{ct})$ to $1000T^{-1}$, where the R_{ct} values were extracted from the Nyquist plots measured at different temperatures (Fig. 3g and Table S4).[64] The calculated E_a value of the Br-Mg anode is 36.65 kJ mol^{-1}, lower than that of bare Mg (49.20 kJ mol^{-1}), indicating a lower energy barrier for Mg^{2+} transport on the Br-Mg interphase layer (Fig. 3g). This reduction in E_a also underscores the crucial role of the Br-Mg interphase layer in promoting ion movement, desolvation, nucleation, and deposition, in contrast to the kinetically sluggish surface of bare Mg.[66,67]

To further elucidate interfacial kinetics and SEI stability during cycling, EIS was performed at various cycle numbers for both bare Mg and Br-Mg anodes (Fig. 3h and S3b). The corresponding Nyquist plots were fitted using the equivalent circuit shown in Fig. S2b, and the extracted impedance parameters are summarized in Table S5. The R_{SEI} indicates the resistance for Mg^{2+} migration through the SEI; after 10 cycles, it is only 2.16 Ω for Br-Mg which is lower than that for bare Mg (3.39 Ω) (Fig. 3i). After prolonged cycling, the R_{SEI} of Br-Mg increased only slightly to 2.96 Ω after 200 cycles. Meanwhile, the R_{SEI} for bare Mg increased drastically to 9.14 Ω after 200 cycles. The increased R_{SEI} in bare Mg anodes leads to higher overpotentials during cycling, ultimately causing short-circuiting. In contrast, the Br-Mg anode maintains a stable R_{SEI} even after extended cycling, reflecting a robust interphase that facilitates faster ion transport, reduces overpotential, and ensures stable cycling performance.

To verify the reversibility of Mg plating/stripping, the symmetric cells were tested at 0.5 mA cm^{-2} and 0.5 mAh cm^{-2} in $Mg[B(hfip)_4]_2$/DME (Fig. 3j). In detail, the magnesium plating and stripping processes in the symmetric cell are each conducted by applying a current density of 0.5 mA cm^{-2} for 1 hour at room temperature (RT = 22 °C) using Mg foil with a thickness of 0.1 mm. The cell with bare Mg short circuited after 796 hours, whereas the Br-Mg anode, benefiting from enhanced surface electrochemical kinetics, sustained stable cycling for 1610 hours (Fig. S4a and b). Furthermore, the voltage hysteresis of the Mg plating/stripping process of bare Mg was as high as ±145 mV, whereas for Br-Mg it was only ±68 mV (Fig. S4c). Furthermore, even when the cycling conditions increased to ten-fold (5 mA cm^{-2} and 5 mAh cm^{-2}), the Br-Mg anode continued to show better reversibility up to 263 hours with a voltage hysteresis as low as ±170 mV (Fig. S4d). In contrast, the bare Mg anode exhibited a low cycling life of only 194 hours with a high voltage hysteresis of ±225 mV. To further validate the stability and functional role of the SEI during cycling, symmetric cells were evaluated at various current densities and areal capacities (Fig. S5a–c). Under all tested conditions, the Br-Mg anode consistently outperformed bare Mg, exhibiting prolonged cycling stability and reduced overpotential. Galvanostatic profiles of three independently assembled symmetric cells using the Br-Mg anode at 3 mA cm^{-2} and 3 mAh cm^{-2} demonstrate robustness and stability of the Br-Mg interphase even under higher operational conditions, and the calculated mean values and standard deviations ensure the reproducibility of symmetric cells (Fig. S5d).

To evaluate the CE of the plating/stripping process, we tested the asymmetric cells fabricated with bare Mg or Br-Mg as the counter electrode and Al/C as the working electrode using the Aurbach CE test (Fig. 3k).[4] A Mg reservoir (Q_T = 5 mAh cm^{-2}) was deposited on the Al/C electrode at a current density of 0.5 mA cm^{-2}, after which the cell was cycled at 0.5 mA cm^{-2} and 0.5 mAh cm^{-2} (Q_C) for 20 cycles. Subsequently, the electrodeposited Mg from the working electrode was stripped by applying a current density of 0.5 mA cm^{-2} until the potential reaches the cut-off potential of 1 V (Q_S) at RT. The average CE was calculated by using eqn (4)

$$CE_{Avg} = (20Q_C + Q_S)/(20Q_C + Q_T) \quad (4)$$

The average CE of bare Mg is only 94.81%, whereas the Br-Mg anode exhibited a significantly enhanced CE of 98.13%. The Aurbach test performed on three independent cells with both bare Mg and Br-Mg anodes (Fig. S6a and b) exhibits consistent voltage profiles and minimal standard deviations, demonstrating the reproducibility and reliability of the electrochemical measurements in asymmetric cells. Furthermore, the

standard deviation of the average CE for the Br-Mg anode is only 0.088, significantly lower than that of bare Mg, which is 0.135, highlighting the enhanced consistency and reliability of Br-Mg anode cycling performance. To ascertain the long-term cycling stability, both anodes were tested in asymmetric cells at 0.5 mA cm^{-2} and 0.5 mAh cm^{-2} (Fig. 3l). In each cycle, magnesium (0.5 mAh cm^{-2}) was first electrodeposited onto the Al/C working electrode by applying a constant current density of 0.5 mA cm^{-2} for 1 h and subsequently stripped by maintaining the same current density until the working electrode potential reaches the cut-off potential of 1.2 V at RT. The cell with a bare Mg anode sustained only 380 cycles, whereas the Br-Mg anode achieved an extended cycling life of 1630 cycles. Moreover, the average CE during prolonged cycling increased from 96.47% for bare Mg to 99.50% for Br-Mg. Even under a sixfold increase of cycling conditions (3 mA cm^{-2} and 3 mAh cm^{-2}), the Br-Mg anode delivered a prolonged cycling life of up to 234 cycles with a high average CE of 99.20% (Fig. S6c). In contrast, bare Mg sustained only 116 cycles with a substantially lower CE of 98.52%. Statistical analysis based on three independent cells shows that the Br-Mg anode exhibits a mean cycling life of 202.3 cycles with a standard deviation of 28.71 (Fig. S6d). Likewise, the mean average CE reaches 99.06% with a narrow standard deviation of 0.14%, underscoring the excellent stability, reproducibility, and robustness of the Br-Mg anode under high current density and large areal capacity conditions.

To benchmark the performance of the Br-Mg anode, we systematically compared it with previously reported artificial interphases on Mg anodes as well as with different boron-centered electrolytes (Fig. 3m–o and Tables S6–S8). In symmetric cells, the Br-Mg anode exhibited significantly enhanced cycling stability, surpassing most previously reported artificial interphases (Fig. 3m and Table S6). These findings highlight the strong potential of the Br-Mg interphase design for broad applicability across diverse Mg electrolytes to effectively mitigate interfacial challenges. Notably, the symmetric-cell performance of the Br-Mg anode in $Mg[B(hfip)_4]_2$/DME electrolyte represents the best reported to date for boron-centered electrolytes, including those employing interface-modified Mg anodes (Fig. 3n and Table S7). Likewise, in asymmetric cells, both cycling stability and CE of the Br-Mg anode surpass all previously reported values for boron-centered electrolytes (Fig. 3o and Table S8).

To ensure the high current application, multi-current tests were carried out both in symmetric and asymmetric cells. The asymmetric cell with Br-Mg exhibited higher CE than bare Mg at all measured currents ranging from 0.5 mA cm^{-2} to 5 mA cm^{-2} (Fig. 4a). Furthermore, when the applied current was reduced back to 0.5 mA cm^{-2} from a high current of 5 mA cm^{-2}, the CE

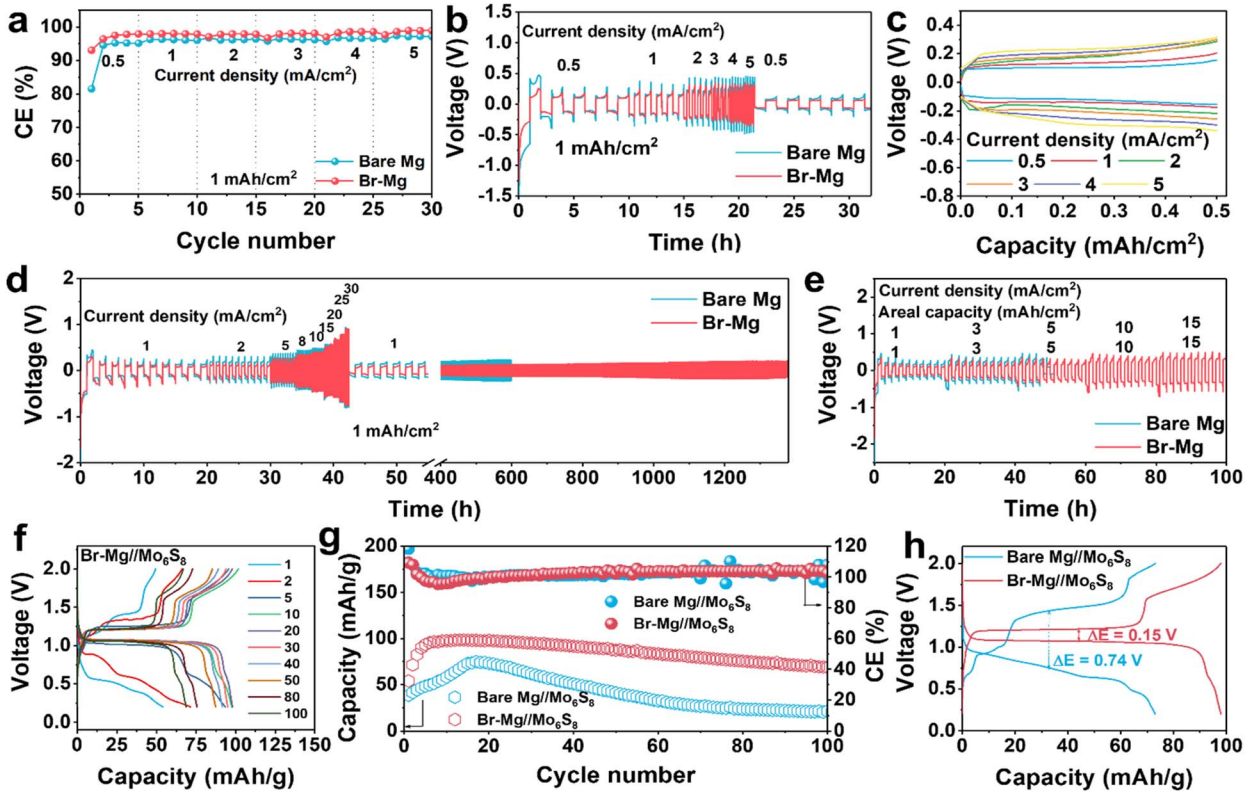

Fig. 4 (a) CE *vs.* cycle number curves of asymmetric cells at different current densities. (b) Galvanostatic cycling profiles of symmetric cells at different applied currents. (c) Voltage profile of the Br-Mg symmetric cell measured at different current densities. (d) Galvanostatic cycling profiles of symmetric cells at different applied currents. (e) Galvanostatic cycling profiles of symmetric cells at different applied current densities and areal capacities. Electrochemical performance of a full cell tested with the Mo_6S_8 cathode: (f) Voltage profile of a full cell measured at 0.1C with the Br-Mg anode. (g) Discharge capacity and CE *vs.* cycle number measured at 0.1C. (h) Voltage profile at the 20th cycle.

values for Br-Mg remained higher than those for bare Mg (Fig. S7). In symmetric cells, Br-Mg showed lower voltage hysteresis than bare Mg at all applied currents (Fig. 4b, c and S8). Furthermore, the cells retained better reversibility when switched back to 0.5 mA cm^{-2} and achieved a longer cycling life of 1600 hours, whereas bare Mg short circuited at around 900 hours (Fig. S9). This justifies that the artificial interphase provides long-term stability even after cycling at high currents. To further validate the robustness of the artificial interphase, symmetric cells were tested up to an extremely high current density of 30 mA cm^{-2} at a fixed areal capacity of 1 mAh cm^{-2} (Fig. 4d). Once again, the cell with Br-Mg exhibited lower voltage hysteresis than bare Mg. Even when the applied current was reduced to 1 mA cm^{-2}, the cell still exhibited better retention of voltage hysteresis and continued to cycle up to a longer time of 1373 hours. Lastly, the symmetric cells with both increasing current density and areal capacity revealed that bare Mg failed at 5 mA cm^{-2} and 5 mAh cm^{-2}, while the Br-Mg anode can cycle up to 15 mA cm^{-2} and 15 mAh cm^{-2} (Fig. 4e). These observations explain the effectiveness of the artificial interphase in inhibiting dendrite growth even at extremely high current density and areal capacity.

To assess the practical viability of the Br-Mg anode, we evaluated the electrochemical performance of full cells assembled with a Mo_6S_8 cathode at a 0.1C rate (Fig. 4f–h and S10). The cell with the Br-Mg anode delivered an initial discharge capacity of 54.01 mAh g^{-1}, significantly higher than that of bare Mg (38.37 mAh g^{-1}). During extended cycling, the Br-Mg cell stabilized more rapidly than the bare Mg counterpart, exhibiting both enhanced capacity and CE. The highest discharge capacity achieved with the Br-Mg anode was 98.40 mAh g^{-1}, surpassing that of bare Mg (74.91 mAh g^{-1}). Notably, the bare

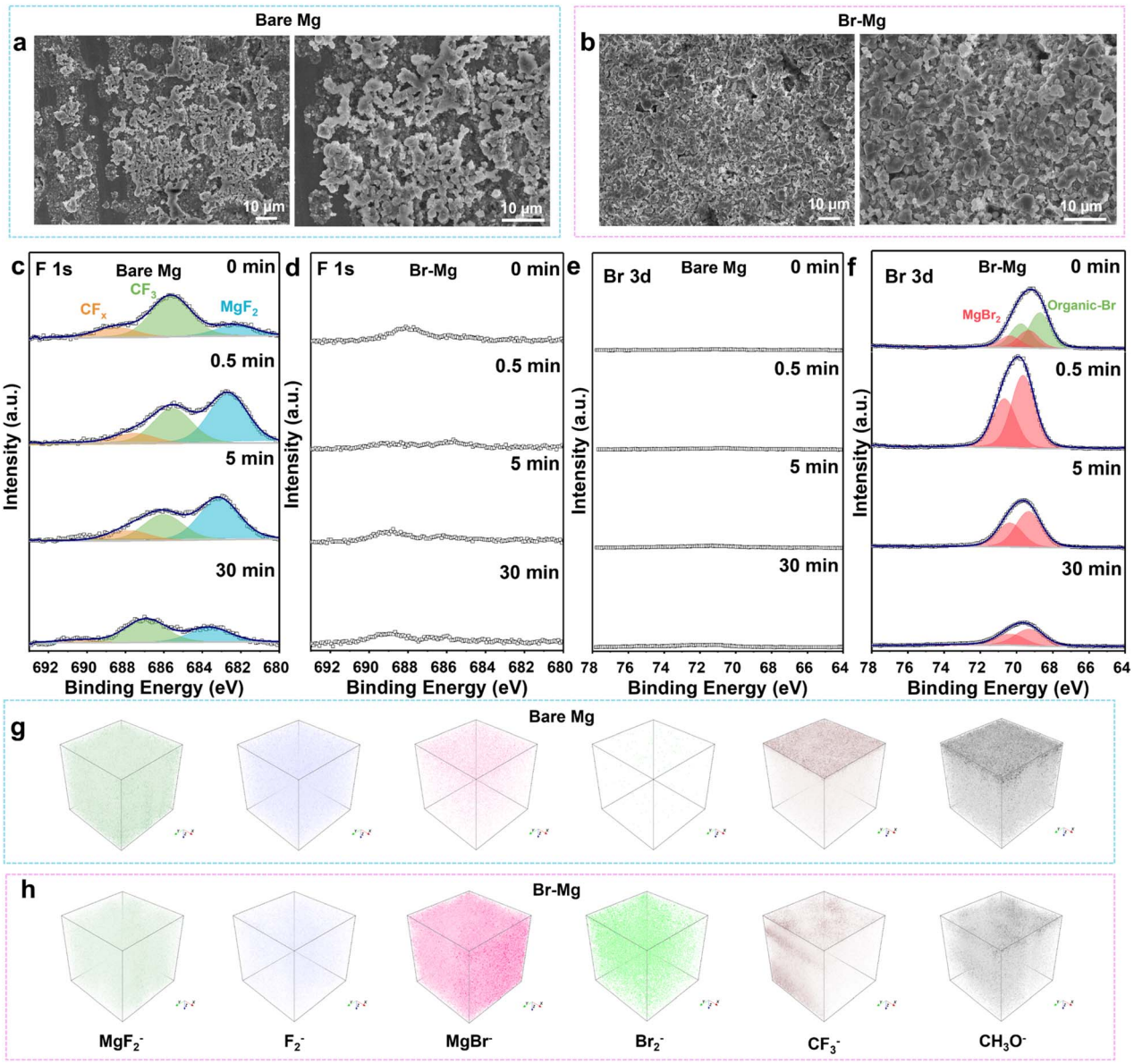

Fig. 5 The structural morphology and surface chemistry of cycled bare Mg and Br-Mg anodes. (a and b) SEM images of cycled anodes. (c–f) Depth profiling XPS analysis of cycled anodes. (g and h) 3D-rendered TOF-SIMS images of cycled anodes.

Mg cell exhibited a large overpotential from the very first cycle, which persisted throughout long-term cycling. By contrast, the Br-Mg cell showed a modest initial overpotential that reduced substantially over subsequent cycles, underscoring the effectiveness of the Br-rich interphase in facilitating more stable interfacial kinetics. The polarization voltage (ΔE), defined as the potential difference at 50% of the charge and discharge capacities, was markedly reduced from 0.74 V for bare Mg to only 0.15 V for Br-Mg in the 20th cycle (Fig. 4h). This substantial decrease in ΔE is attributed to enhanced surface kinetics at the anode enabled by the artificial interphase. In contrast, the larger ΔE observed for bare Mg arises from the continuous accumulation of electrolyte degradation species on the anode.[55]

The structural morphology and surface chemistry of cycled anodes were measured in the retrieved anodes from symmetric cells after 20 cycles at 0.5 mA cm^{-2} and 0.5 mAh cm^{-2}, using SEM, XPS, and TOF-SIMS. The SEM images of electrodeposited Mg on anodes revealed that the bare Mg anode (Fig. 5a) exhibited irregular deposits with numerous voids, whereas the Br-Mg anode (Fig. 5b) displayed a homogeneous and compact morphology, highlighting the role of the Br-rich artificial interphase in regulating nucleation and suppressing uncontrolled growth. Depth profiling XPS analysis of the cycled anodes (Fig. 5c–f and S11) provides crucial insights into the chemical composition of the SEI formed after cycling. The Mg 2p spectra of cycled anodes show that, for both the anodes, the dominant SEI components were indexed as $MgBr_2/MgF_2/MgO$ (Fig. S11 and Table S9). To delineate the specific contributions of each species, the F 1s and Br 3d spectra were examined in detail (Fig. 5c–f). The F 1s spectra of the bare Mg anode revealed pronounced signals corresponding to CF_x, CF_3, and MgF_2 at the surface, indicative of extensive electrolyte decomposition and the accumulation of electrolyte-derived SEI products (Fig. 5c). In contrast, the Br-Mg anode displayed featureless F 1s spectra across all etching depths, confirming the absence of such decomposition products within the SEI (Fig. 5d). Consistently, the Br 3d spectra of bare Mg remained flat throughout all etching times, verifying the absence of Br-containing species and establishing that its SEI is primarily composed of F and O species (Fig. 5e). Moreover, the presence of dangling bonds in the Mg 2p spectra of bare Mg further indicates the formation of a defective Mg–O terminated layer, whereas no such feature was observed in the Br-Mg electrode.[61] By contrast, the Br 3d spectra of the cycled Br-Mg anode revealed a Br-rich interphase dominated by $MgBr_2$, with only surface contributions from organic Br species (Fig. 5f and Table S10). Collectively, these results demonstrate that the SEI on Br-Mg is chemically enriched in Br species, principally $MgBr_2$, whereas the SEI on bare Mg is largely comprised of electrolyte decomposition products. The 3D rendered TOF-SIMS images (Fig. 5g and h) further corroborate the distinct SEI chemistries of the two anodes. The bare Mg electrode exhibited a high concentration of fluorine-rich species, together with abundant electrolyte decomposition fragments such as CF_3^- and CH_3O^-, consistent with XPS observations that the SEI is primarily composed of MgF_2. By contrast, the Br-Mg electrode displayed a Br-rich SEI dominated by $MgBr_2$, with significantly lower concentrations of electrolyte decomposition-derived fragments. Unlike the bare Mg anode, where uncontrolled electrolyte degradation drives the formation of a low ionic-conducting MgF_2-rich SEI, the $MgBr_2$-rich artificial interphase inherently functions as a stable SEI, offering superior ionic conductivity. This protective interphase effectively shields the anode from electrolyte decomposition during cycling while simultaneously facilitating rapid interfacial desolvation. Collectively, the combined SEI characterization and electrochemical analyses demonstrate that a homogeneous, Br-rich inorganic SEI enables uniform Mg^{2+} transport while effectively suppressing interfacial degradation. In contrast, bare Mg anodes form a heterogeneous and highly resistive SEI dominated by oxide/hydroxide and flouride species, resulting in continuous impedance growth, non-uniform Mg deposition, and accelerated performance decay. This deliberate compositional and structural optimization of a Br-rich inorganic SEI underpins the enhanced interfacial conductivity and long-term durability of the Br-Mg anode, offering clear design principles for the development of high-performance Mg metal interfaces.

Conclusions

In summary, we demonstrate the fabrication of a Br-rich artificial interphase on a Mg metal anode that evidently enhances cycling stability and CE in boron-centered Mg electrolyte. The Br-rich artificial interphase accelerates interfacial charge-transfer kinetics, suppresses electrolyte decomposition on the anode surface, and regulates Mg electrodeposition morphology to be highly homogeneous. As a result, the cycling life of symmetric cells improved from 796 to 1610 hours. In asymmetric cells, the CE of the Mg plating/stripping process significantly improved from 96.47% to 99.50%, concurrently extending the cycling life from 380 to 1630 cycles, thereby underscoring the efficacy of the Br-rich interphase in enabling near-ideal reversibility. Furthermore, full cells assembled with a Mo_6S_8 cathode delivered higher capacities, reduced polarization voltage, and superior reversibility when paired with the Br-Mg anode, underscoring the critical role of surface kinetics in dictating device-level performance. Collectively, these findings highlight the transformative potential of artificial interphases in overcoming interfacial instabilities and advancing the practical deployment of Mg batteries.

Author contributions

D. C. and G. Y. contributed equally to this work. D. C., G. Y., and Z. W. S. conceived the original idea. D. C. and G. Y. performed the experiments. S. S. and S. K. contributed to review and editing of the manuscript. J. W. performed the XRD measurements. Z. X. performed the TOF-SIMS experiments. D. H. L. S. performed the XPS measurements. Z. S. provided the Mo_6S_8 cathode materials. Z. W. S. supervised the project, edited the original draft, and provided financial support.

Conflicts of interest

There are no conflicts to declare.

Data availability

The data supporting this article have been included as part of the supplementary information (SI). Supplementary information: experimental methods, cross-sectional SEM image, equivalent circuits employed to fit Nyquist plots, Nyquist plots measured under different temperatures and cycles, galvanostatic cycling profiles of symmetric cells at different conditions, galvanostatic cycling profiles of asymmetric cells at different conditions, voltage profile of full cell, depth profiling XPS spectra, fitting parameters of XPS spectra and Nyquist plots, comparison tables of performances of symmetric and asymmetric cells. See DOI: https://doi.org/10.1039/d5ta08003g.

Acknowledgements

Z. W. S. was supported by the Singapore National Research Foundation (NRF Investigatorship NRF-NRFI09-0002) and the Agency for Science, Technology and Research (MTC Programmatic Fund M23L9b0052).

References

1 Y. Sun, F. Ai and Y. C. Lu, *Small*, 2022, **18**, e2200009.
2 Y. Li, S. Kumar, G. Yang, J. Lu, Y. Yao, K. Kang and Z. W. Seh, *Science*, 2025, **389**, eadl5482.
3 Y. Chen, X. Shen, J. Wang, Y. Zhang, Y. Hao, L. Tong, G. Huang, Q. Li, X. Zhou, B. Qu and F. Pan, *ACS Energy Lett.*, 2024, **9**, 5616–5626.
4 D. Chinnadurai, S. Kumar, C. Zhang, M.-F. Ng, Y. Li, J. Wang, T. Ghosh, G. Yang, Z. Xing, W. Liu and Z. W. Seh, *Adv. Energy Mater.*, 2025, **15**, 2500979.
5 T. D. Gregory, R. J. Hoffman and R. C. Winterton, *J. Electrochem. Soc.*, 1990, **137**, 775.
6 D. Aurbach, Z. Lu, A. Schechter, Y. Gofer, H. Gizbar, R. Turgeman, Y. Cohen, M. Moshkovich and E. Levi, *Nature*, 2000, **407**, 724–727.
7 O. Mizrahi, N. Amir, E. Pollak, O. Chusid, V. Marks, H. Gottlieb, L. Larush, E. Zinigrad and D. Aurbach, *J. Electrochem. Soc.*, 2008, **155**, A103.
8 Z. Zhao-Karger, X. Zhao, O. Fuhr and M. Fichtner, *RSC Adv.*, 2013, **3**, 16330–16335.
9 Y. Yang, W. Wang, Y. Nuli, J. Yang and J. Wang, *ACS Appl. Mater. Interfaces*, 2019, **11**, 9062–9072.
10 S. Y. Ha, Y. W. Lee, S. W. Woo, B. Koo, J. S. Kim, J. Cho, K. T. Lee and N. S. Choi, *ACS Appl. Mater. Interfaces*, 2014, **6**, 4063–4073.
11 C. Liao, N. Sa, B. Key, A. K. Burrell, L. Cheng, L. A. Curtiss, J. T. Vaughey, J.-J. Woo, L. Hu and B. Pan, *J. Mater. Chem. A*, 2015, **3**, 6082–6087.
12 R. K. Bhardwaj and A. J. Bhattacharyya, *ACS Appl. Energy Mater.*, 2021, **4**, 14121–14128.
13 R. Horia, D. T. Nguyen, A. Y. S. Eng and Z. W. Seh, *Nano Lett.*, 2021, **21**, 8220–8228.
14 D. Chinnadurai, W. Y. Lieu, S. Kumar, G. Yang, Y. Li and Z. W. Seh, *Nano Lett.*, 2023, **23**, 1564–1572.
15 D. Huang, S. Tan, M. Li, D. Wang, C. Han, Q. An and L. Mai, *ACS Appl. Mater. Interfaces*, 2020, **12**, 17474–17480.
16 D.-T. Nguyen, A. Y. S. Eng, M.-F. Ng, V. Kumar, Z. Sofer, A. D. Handoko, G. S. Subramanian and Z. W. Seh, *Cell Rep. Phys. Sci.*, 2020, **1**, 100265.
17 D.-T. Nguyen, A. Y. S. Eng, R. Horia, Z. Sofer, A. D. Handoko, M.-F. Ng and Z. W. Seh, *Energy Storage Mater.*, 2022, **45**, 1120–1132.
18 N. Sa, B. Pan, A. Saha-Shah, A. A. Hubaud, J. T. Vaughey, L. A. Baker, C. Liao and A. K. Burrell, *ACS Appl. Mater. Interfaces*, 2016, **8**, 16002–16008.
19 X. Li, T. Gao, F. Han, Z. Ma, X. Fan, S. Hou, N. Eidson, W. Li and C. Wang, *Adv. Energy Mater.*, 2017, **8**, 1701728.
20 J. Zhang, X. Guan, R. Lv, D. Wang, P. Liu and J. Luo, *Energy Storage Mater.*, 2020, **26**, 408–413.
21 L. C. Merrill and J. L. Schaefer, *Chem. Mater.*, 2018, **30**, 3971–3974.
22 J. Xiao, X. Zhang, H. Fan, Q. Lin, Z. S. Ng, W. Chen and Y. Zhang, *ACS Appl. Mater. Interfaces*, 2024, **16**, 17673–17682.
23 Y. Du, Y. Chen, S. Tan, J. Chen, X. Huang, L. Cui, J. Long, Z. Wang, X. Yao, B. Shang, G. Huang, X. Zhou, L. Li, J. Wang and F. Pan, *Energy Storage Mater.*, 2023, **62**, 102939.
24 C. Li, R. D. Guha, S. D. House, J. D. Bazak, Y. Yu, L. Zhou, K. Zavadil, K. A. Persson and L. F. Nazar, *Joule*, 2025, **9**, 101790.
25 S. Fan, G. M. Asselin, B. Pan, H. Wang, Y. Ren, J. T. Vaughey and N. Sa, *ACS Appl. Mater. Interfaces*, 2020, **12**, 10252–10260.
26 M. Wang, W. Sun, K. Zhang, Z. Zhang, A. Du, S. Dong, J. Zhang, J. Liu, X. Chen, Z. Zhou, F. Li, Z. Li, G. Li and G. Cui, *Energy Environ. Sci.*, 2024, **17**, 630–641.
27 R. Horia, D. T. Nguyen, A. Y. S. Eng and Z. W. Seh, *Batter. Supercaps*, 2022, **5**, e202200011.
28 G. Yang, Y. Li, C. Zhang, J. Wang, Y. Bai, C. Y. J. Lim, M. F. Ng, Z. Chang, S. Kumar, Z. Sofer, W. Liu and Z. W. Seh, *Nano Lett.*, 2022, **22**, 9138–9146.
29 G. Yang, Y. Li, J. Wang, Y. Lum, C. Y. J. Lim, M.-F. Ng, C. Zhang, Z. Chang, Z. Zhang, A. D. Handoko, T. Ghosh, S. Li, Z. Sofer, W. Liu, Y. Yao and Z. W. Seh, *Energy Environ. Sci.*, 2024, **17**, 1141–1152.
30 Y. Cheng, R. M. Stolley, K. S. Han, Y. Shao, B. W. Arey, N. M. Washton, K. T. Mueller, M. L. Helm, V. L. Sprenkle, J. Liu and G. Li, *Phys. Chem. Chem. Phys.*, 2015, **17**, 13307–13314.
31 L. Yang, C. Yang, Y. Chen, Z. Pu, Z. Zhang, Y. Jie, X. Zheng, Y. Xiao, S. Jiao, Q. Li and D. Xu, *ACS Appl. Mater. Interfaces*, 2021, **13**, 30712–30721.
32 Y. Sun, Y. Wang, L. Jiang, D. Dong, W. Wang, J. Fan and Y.-C. Lu, *Energy Environ. Sci.*, 2023, **16**, 265–274.
33 R. Lv, X. Guan, J. Zhang, Y. Xia and J. Luo, *Natl. Sci. Rev.*, 2020, **7**, 333–341.
34 Y. Li, P. Zuo, R. Li, H. Huo, Y. Ma, C. Du, Y. Gao, G. Yin and R. S. Weatherup, *ACS Appl. Mater. Interfaces*, 2021, **13**, 24565–24574.

35 R. Zhang, C. Cui, R. Li, Y. Li, C. Du, Y. Gao, H. Huo, Y. Ma, P. Zuo and G. Yin, *Chem. Eng. J.*, 2021, **426**, 130751.
36 Y. Zhao, A. Du, S. Dong, F. Jiang, Z. Guo, X. Ge, X. Qu, X. Zhou and G. Cui, *ACS Energy Lett.*, 2021, **6**, 2594–2601.
37 Y. Li, X. Zhou, J. Hu, Y. Zheng, M. Huang, K. Guo and C. Li, *Energy Storage Mater.*, 2022, **46**, 1–9.
38 Y. Wang, E. Sahadeo and S. B. Lee, *ACS Appl. Energy Mater.*, 2022, **5**, 2613–2620.
39 Y. Zhang, J. Li, W. Zhao, H. Dou, X. Zhao, Y. Liu, B. Zhang and X. Yang, *Adv. Mater.*, 2022, **34**, e2108114.
40 Y. Zhuang, D. Wu, F. Wang, Y. Xu, J. Zeng and J. Zhao, *ACS Appl. Mater. Interfaces*, 2022, **14**, 47605–47615.
41 A. R. Jeon, S. Jeon, G. Lim, J. Jang, W. J. No, S. H. Oh, J. Hong, S. H. Yu and M. Lee, *ACS Nano*, 2023, **17**, 8980–8991.
42 S. Shin, J. H. Kwak, S. H. Oh, H. S. Kim, S. H. Yu and H. D. Lim, *ACS Appl. Mater. Interfaces*, 2023, **15**, 28684–28691.
43 C. Wang, H. Huang, X. Wu, M. Yousaf, M. Yan and Y. Jiang, *ACS Appl. Mater. Interfaces*, 2023, **15**, 51126–51134.
44 D. Zhang, Y. Sun, X. Liu, Y. Zhang, R. Wang, Y. Zhao, M. Pan, Y. Wang, S. Chen, M. Zhou, Y. Chen, J. Yang, J. Wang and Y. NuLi, *ACS Energy Lett.*, 2024, **9**, 2685–2695.
45 A. Du, Z. Zhang, H. Qu, Z. Cui, L. Qiao, L. Wang, J. Chai, T. Lu, S. Dong, T. Dong, H. Xu, X. Zhou and G. Cui, *Energy Environ. Sci.*, 2017, **10**, 2616–2625.
46 Z. Zhao-Karger, M. E. G. Bardaji, O. Fuhr and M. Fichtner, *J. Mater. Chem. A*, 2017, **5**, 10815–10820.
47 J. Luo, Y. Bi, L. Zhang, X. Zhang and T. L. Liu, *Angew Chem. Int. Ed. Engl.*, 2019, **58**, 6967–6971.
48 X. Song, J. Sun, W. Ren, L. Wang, B. Yang, H. Ning, P. Zhang, Z. Caixiang, Z. Tie, X. Zhang, Y. NuLi and Z. Jin, *Angew Chem. Int. Ed. Engl.*, 2025, **64**, e202417450.
49 S. Li, J. Zhang, S. Zhang, Q. Liu, H. Cheng, L. Fan, W. Zhang, X. Wang, Q. Wu and Y. Lu, *Nat. Energy*, 2024, **9**, 285–297.
50 K. Tang, A. Du, S. Dong, Z. Cui, X. Liu, C. Lu, J. Zhao, X. Zhou and G. Cui, *Adv. Mater.*, 2020, **32**, 1904987.
51 C. Chen, J. Chen, S. Tan, Z. Gao, X. Huang, Z. He, J. Huang, R. Deng, F. Xiong, G. Huang, J. Wang, L. Li and F. Pan, *Adv. Funct. Mater.*, 2025, 2505843.
52 Z. Meng, Z. Li, L. Wang, T. Diemant, D. Bosubabu, Y. Tang, R. Berthelot, Z. Zhao-Karger and M. Fichtner, *ACS Appl. Mater. Interfaces*, 2021, **13**, 37044–37051.
53 Z. Li, T. Diemant, Z. Meng, Y. Xiu, A. Reupert, L. Wang, M. Fichtner and Z. Zhao-Karger, *ACS Appl. Mater. Interfaces*, 2021, **13**, 33123–33132.
54 B. Dlugatch, J. Drews, R. Attias, B. Gavriel, A. Ambar, T. Danner, A. Latz and D. Aurbach, *J. Electrochem. Soc.*, 2023, **170**, 090542.
55 S. Cao, X. Qi and X. Zhao, *Energy Fuels*, 2025, **39**, 15498–15504.
56 Y. Chen, Y. Zhang, Z. Tang, Z. Zhang, L. Tong, X. Gan, X. Shen, G. Huang, Q. Li, B. Qu, F. Pan and J. Wang, *Chem. Eng. J.*, 2025, **521**, 166781.
57 D. Seyferth, *Organometallics*, 2009, **28**, 1598–1605.
58 R. M. Peltzer, J. Gauss, O. Eisenstein and M. Cascella, *J. Am. Chem. Soc.*, 2020, **142**, 2984–2994.
59 E. Sheha, *J. Adv. Res.*, 2016, **7**, 29–36.
60 D. Chinnadurai, A. R. Selvaraj, R. Rajendiran, G. R. Kumar, H.-J. Kim, K. K. Viswanathan and K. Prabakar, *ACS Omega*, 2018, **3**, 1718–1725.
61 D. Chinnadurai, Y. Li, C. Zhang, G. Yang, W. Y. Lieu, S. Kumar, Z. Xing, W. Liu and Z. W. Seh, *Nano Lett.*, 2023, **23**, 11233–11242.
62 T. Wen, B. Qu, S. Tan, G. Huang, J. Song, Z. Wang, J. Wang, A. Tang and F. Pan, *Energy Storage Mater.*, 2023, **55**, 816–825.
63 X. Peng, Y. Yuan, D. Gu, D. Li, L. Wu, L. Zhang, G. Huang, J. Wang and F. Pan, *Adv. Funct. Mater.*, 2025, 2422278.
64 G. Li, K. Chen, M. Lei, T. Wang, M. Hu and C. Li, *Adv. Energy Mater.*, 2024, **14**, 2401507.
65 Y. Li, G. Yang, C. Zhang, W. Y. Lieu, C. Y. J. Lim, S. Sun, J. Wang, S. Jiang, Z. Xing, Z. Sofer, M. F. Ng, W. Liu and Z. W. Seh, *Adv. Funct. Mater.*, 2023, **33**, 2210639.
66 J. Bi, J. Li, Z. Zhou, B. Li, K. Wang, G. Gao, Z. Du, W. Ai and W. Huang, *Adv. Mater.*, 2025, e2502098.
67 J. Bi, X. Huo, Z. Zhou, J. Li, K. Wang, Z. Du and W. Ai, *Inorg. Chem. Front.*, 2025, **12**, 3653–3662.